Title

Effective water disinfection using magnetic barium phosphate nanoflakes loaded with Ag nanoparticles

Authors

Zhang, Fan
Lee, Meng Hao
Huang, Yuxiong
et al.

Publication Date

2019-05-01

DOI

10.1016/j.jclepro.2019.01.232

Peer reviewed

Journal of Cleaner Production 218 (2019) 173–182

Contents lists available at ScienceDirect

Journal of Cleaner Production

journal homepage: www.elsevier.com/locate/jclepro

Effective water disinfection using magnetic barium phosphate nanoflakes loaded with Ag nanoparticles

Fan Zhang [a, *], Meng Hao Lee [b], Yuxiong Huang [c, 1], Arturo A. Keller [c], Sanghamitra Majumdar [c], Pabel Cervantes-Avilés [c], Xiaoxiu Tang [a], Siqiao Yin [d]

[a] College of Sciences, Nanjing Agricultural University, Nanjing 210095, PR China
[b] Department of Chemical Engineering, University of California, Santa Barbara, CA 93106, USA
[c] Bren School of Environmental Science and Management, University of California, Santa Barbara, CA 93106, USA
[d] Department of Chemistry & Biochemistry, University of California, Santa Barbara, CA 93106, USA

ARTICLE INFO

Article history:
Received 12 October 2018
Received in revised form
20 December 2018
Accepted 19 January 2019
Available online 31 January 2019

Keywords:
Ag NPs loaded magnetic nanoflake
E. coli adsorption
Disinfection
Reusability
Water treatment

ABSTRACT

In this work, novel magnetic nanocomposites, Fe_3O_4@$Ba_3(PO_4)_2$ (denominated FBP) nanoflakes loaded with Ag nanoparticles (NPs) (denominated FBPA), were reported for cleaning *E. coli* from water. FBPA with 1 wt% Ag (denominated FBPA1) showed a higher adsorption efficiency (94%) than FBPA with 10 wt% Ag (denominated FBPA10), for water heavily contaminated with *E. coli* (5×10^8 CFU/mL), both at a dosage of 1 g/L within 10 min. Importantly, the loaded Ag NPs can greatly improve the disinfection effect of FBP due to the great antimicrobial activity of Ag NPs via the released Ag^+. Confocal fluorescent images and dilution plating results showed that ~100% of *E. coli* could be inactivated by FBPA1 within 10 min. The calculated disinfection capacity was higher than some other materials. Three co-existed salts in solutions decreased the disinfection efficiency of FBPA1 to be ~67% (NaCl), ~59% ($CaCl_2$), and ~41% ($MgCl_2$). Furthermore, FBPA1 can be reclaimed via a magnet to be reused. FBPA1 maintained an adsorption efficiency of 86%, disinfection effect of 70%, and ~90% of loaded Ag NPs after the fifth recover and reuse cycle.

1. Introduction

Nowadays, the removal of various contaminants, for instance, organic matters, microorganisms, and heavy metals is a priority for ensuring a safe and clean water system (Sharma et al., 2018). Reliable access to clean water devoid of microorganisms is one of these major global health issues (Sharma et al., 2015). *Escherichia coli* (*E. coli*) is usually acted as an indicator of microorganism contamination to monitor water quality (Zhan et al., 2015). Though many technologies have been employed to remove *E. coli* from solution, currently applied water treatment methods are still not able to provide the water quality and demand with a low cost to meet improved requirements of the environment and human health (Schwarzenbach et al., 2006; Sedlak and von Gunten, 2011). Therefore, different materials were developed as cleaner productions to fulfill next-generation demand of effective, cost-effective, or sustainable disinfection in water treatment (Boholm and Arvidsson, 2014; Gupta et al., 2015; Raza et al., 2015; Thakur et al., 2017).

It is well known that Ag NPs exhibit broad-spectrum antimicrobial activity with relative non-toxic properties to human cells (Lee et al., 2005). However, either the Ag NPs themselves or their ability to deliver dissolved Ag^+ can directly lead to growth inhibition and cell damage toward bacteria (Yin et al., 2011). Two main disinfection mechanisms of Ag NPs have been proposed in previous studies: (1) reactive oxygen species (ROS) formed at the surface of Ag NPs can generate oxidative stress to membrane and then cause cell damage (Choi and Hu, 2008; Hwang et al., 2008); (2) released Ag^+ can interact with vital enzymes and proteins, affect the function of membranes, and then result in ultimate cell death (Levard et al., 2012; Ratte, 1999). Notably, the aggregation of Ag NPs in the

* Corresponding author.
E-mail addresses: zhangfan0128@njau.edu.cn (F. Zhang), menghaolee@umail.ucsb.edu (M.H. Lee), yhuang@bren.ucsb.edu (Y. Huang), keller@bren.ucsb.edu (A.A. Keller), majumdarsm@gmail.com (S. Majumdar), pabel.cervantes@gmail.com (P. Cervantes-Avilés), 2017811042@njau.edu.cn (X. Tang), siqiao@umail.ucsb.edu (S. Yin).
[1] Present address. Shenzhen Environmental Science and New Energy Technology Engineering Laboratory, Tsinghua-Berkeley Shenzhen Institute, Shenzhen 518055, PR China.

https://doi.org/10.1016/j.jclepro.2019.01.232
0959-6526/

aqueous medium may hinder their antimicrobial properties (Kumar and Munstedt, 2005). Therefore, to fabricate Ag NPs on a support material is highly desirable to inhibit their aggregation and biofilm formation (Das et al., 2013). A large variety of supportive materials have been developed to fabricate Ag NPs for water disinfection or biofouling control, like graphene oxide-silver nanocomposites (Song et al., 2016), nano-silica fabricated with Ag NPs (Das et al., 2013), magnetic bimetallic Fe–Ag NPs (Markova et al., 2013), Ag-iron oxide/fly ash (Joshi et al., 2015), Ag–$CoFe_2O_4$-GO nanocomposite (Ma et al., 2015), Ag NPs decorated Fe_3O_4@SiO_2 core-shell nanosphere (Singh and Bahadur, 2015), Ag/BiOI composite (Zhu et al., 2012). These materials presented good antimicrobial properties. Importantly, some of them can be r from water via a magnetic field, which may avoid secondary pollution and potential environmental risk resulting from the pollutants-accumulated materials left in the water after treatment (Ma et al., 2015).

Phosphate or apatite based nanomaterials, which are antimicrobial and cost-effective (Han et al., 1998; Kolmas et al., 2014; Ravi et al., 2012), have gained increasing attention as a preferred support material for the fabrication of composite Ag NPs. For example, an Ag–TiO_2/HAP/Al_2O_3 composite membrane that provides microfiltration integrated with photocatalysis was used for humic acid removal and anti-fouling (Ma et al., 2010); hydroxyapatite-supported Ag–TiO_2 was employed as an *E. coli* disinfection photocatalyst (Reddy et al., 2007); and apatite-coated Ag/AgBr/TiO_2 was used as visible-light photocatalyst for destruction of bacteria (Elahifard et al., 2007). However, despite the successful disinfection provided by these materials, they cannot be easily separated from the water system after treatment, which may lead to environmental and safety concerns. Embedding Fe_3O_4 NPs in the Ag-phosphate nanocomposites instead of TiO_2 may allow a simple magnetic separation after treatment. Importantly, Fe_3O_4 NPs possess flocculation (Song et al., 2018) and protein oxidation effect towards bacteria (Inbaraj et al., 2012; Singh et al., 2011; Tran et al., 2010) which may lead to more effective bacteria adsorption and disinfection process.

Very recently, a cost-effective magnetic Fe_3O_4 barium phosphate (FBP) nanoflake was reported to be effective in adsorption and disinfection of *E. coli*. (Song et al., 2018). In the present work, a simple, green synthesis method has been developed to load Ag NPs on the surface of the FBP nanoflakes through reduction of Ag^+ and then deposition of Ag^0. The FBP with 1 wt% Ag (denominated FBPA1) and 10 wt% Ag (denominated FBPA10) were characterized thoroughly. The bacterial adsorption and disinfection efficiency of these two novel materials were analyzed in comparison with FBP. Their performance in the presence of common ions and reusability were also investigated in detail.

2. Experimental

2.1. Reagents

Analytical grade barium nitrate, sodium phosphate, silver nitrate, sodium borohydride, magnesium chloride, sodium chloride, calcium chloride, nitric acid, and sodium hydroxide was purchased from Sigma-Aldrich and used as received.

2.2. Material synthesis

Synthesis of FBP nanocomposites. Fe_3O_4 NPs (size of ~100 nm) were obtained according to previous work (Song et al., 2018). The magnetic FBP nanoflakes were prepared through a simple hydrothermal method without toxic reagents and organic solvents. First, 0.06 g Fe_3O_4 NPs and 7.5 mmol barium nitrate were ultrasonically dispersed into 40 mL of deionized (DI) water for 15 min at 30 °C. Sodium phosphate (5 mmol) was dissolved in 10 mL of DI water and then added dropwise slowly into the Fe_3O_4/$Ba(NO_3)_2$ suspension. After mechanical stirring for 30 min, the fully mixed solution was transferred into two 50 mL Teflon bottles and then held and sealed in two stainless-steel autoclaves. The autoclaves were maintained at 200 °C for 5 h and then cooled to 25 °C. The obtained powder from autoclaves was washed by DI water and ethanol successively and then dried in a vacuum oven at 50 °C for 4 h.

Synthesis of FBPA1 and FBPA10. For a typical synthesis, 1.0 g of FBP was suspended in 10 mL DI water in two separate 20 mL scintillation tubes and sonicated for 5 min. Then, 0.18 mL or 1.8 mL of $AgNO_3$ aqueous solution (0.5 M) was added to the tubes to obtain 1 wt% or 10 wt% mass ratio of Ag to FBP. Next, 2 mL of ice-cold $NaBH_4$ (100 mM) was rapidly injected into the mixture, stirring vigorously and generating a brown solution. The whole solution was stirred slowly for 3 h at room temperature (25 °C) to promote the decomposition of the remaining $NaBH_4$ in solution. The product was centrifuged at 4000 rpm for 10 min and washed with DI water and ethanol, then dried in a vacuum oven at 50 °C for 3 h. After the synthesis, around 1.0 g FBPA1 or FBPA10 were obtained at a low material cost of about $0.21-$0.34/g.

2.3. Characterization

The composition and crystal phase of the obtained samples were determined with X-ray diffraction (XRD, Panalytical Empyrean powder diffractometer) by depositing the sample on a glass substrate. The size and morphology of as-prepared samples were characterized by scanning electron microscopy (SEM, FEI Nova Nano 650) with a field-emission electron gun. The high-resolution transmission electron microscopic (HRTEM) observations and electron dispersive X-ray spectrometer (EDX) were performed on a FEI Tecnai G2 Sphera microscope operated at 200 kV. The infrared spectroscopy (IR) were recorded by using a Thermo Nicolet iS10 FTIR spectrometer in the wavelength range from 500 to 4500 nm. For the magnetic measurements, the hysteresis loops were measured on the continuous films at $T = 300$ K using a Dynacool physical property measurement system (PPMS) (maximum applied field±12T). BET surface areas were determined via N_2 physisorption using a Micromeritics 3 Flex Physisorption. Concentrations of Ag leaching in the solution were determined by inductively coupled plasma mass spectroscopy (ICP-MS, Agilent 7900). The corresponding Zeta potential (ZP) of the samples were studied by a ZP analyzer (Malvern, Model Nano ZS). The concentration of the *E. coli* suspension was evaluated by measuring the optical density at 600 nm (OD600) with an ultraviolet spectrophotometer (Shimadzu, model UV1700). The fluorescent-based cell live and dead test was conducted on a fluorescent microscopy (Leica SP8 Resonant Scanning Confocal).

2.4. Bacteria suspension preparation

A kanamycin resistant *E. coli* strain was cultivated in 20 mL of Luria Broth (LB) growth medium which consisted of 5 g/L bacto-yeast extract, 10 g/L tryptone, 50 μg/mL kanamycin, and 10 g/L NaCl. The strain was shaken at 37 °C in a thermostatic incubator at 220 rpm until reached the logarithmic growth late phase. The bacterial suspension was re-suspended in 0.85 wt% NaCl and then the bacterial stock solution with an initial cell density of about 5×10^8 CFU/mL was obtained.

2.5. Adsorption and disinfection toward E. coli

Generally, the adsorption and disinfection efficiency of FBP, FBPA1 or FBPA10 were investigated by adding 0.05 g of material into 50 mL of *E. coli* suspension (5×10^8 CFU/mL) at 25 °C and pH

6.0 under mechanical stirring at 220 rpm for 30 min. To evaluate the effect of commonly co-existed ions in water system on disinfection efficiency by materials, three kinds of salts ($CaCl_2$, $MgCl_2$, and NaCl) were dissolved in 50 mL of DI water (pH 6) to obtain solutions with cation concentrations of 5, 10, 20, 50, and 100 mg/L. The leaching of Ag^+ after 5 days of suspending 0.05 g of FBPA1 in 50 mL of these salt solutions was analyzed by ICP-MS. The disinfection efficiency of FBPA1 with a cation concentration of 2 mg/L was investigated via confocal fluorescent images. After treatment, the bacteria-loaded material could be separated from the aqueous solution by a neodymium magnet and then the reclaimed materials were reused for 5 cycles at the same experimental conditions without regeneration. All experimental operations were repeated three times and the average results are reported. The detailed experimental methods of confocal fluorescent images and dilution plate count are described in the Supporting Information.

3. Results and discussion

3.1. Characterization of materials

The SEM image of FBPA1 is shown in Fig. 1a. A flake-like structure with a thickness of ~50 nm was observed, and the length (~4 μm) is larger than that of an *E. coli* cell (700 nm-1.2 μm) (Ma et al., 2015). Some small NPs (50–100 nm) were found loaded on the surface of FBPA1 (Fig. 1b), which were absent in the FBP nanoflake (Fig. S1). Energy dispersive X-ray spectroscopy (EDS) results (Fig. 1b) demonstrated the presence of Fe (2.95 wt%) and Ag (0.94 wt%) in the as-prepared FBPA1. As shown in Fig. 1c and d, FBPA10 nanoflakes were covered by more small NPs than FBPA1, and the higher loading of Ag (8.79 wt%) was confirmed by EDS results. The element mapping results (Fig. S2) showed that Ag, Fe, Ba, and P were all uniformly presented on the nanoflake, implying the loaded NPs may be nanocomposites containing both Fe and Ag. The surface area of FBPA1 was 11.5 m^2/g with a Barrett-Joyner-Halenda (BJH) adsorption cumulative pore volume of 0.053 cm^3/g. FBPA10 possess a higher surface area of 12.2 m^2/g and BJH adsorption cumulative pore volume of 0.062 cm^3/g, which may be beneficial to disinfection control due to more exposed active sites (Song et al., 2018).

The morphology and structure of FBPA1 and FBPA10 were further studied by TEM (Fig. 2). FBPA1 and FBPA10 show thin nanoflake structure with sharp edges and corners. NPs with different sizes were found adhered to the surface, similar to SEM results. The NPs with an average size of ~100 nm which were assembled and adhered to the surface of FBP nanoflake is Fe_3O_4 NPs (Song et al., 2018). Smaller dark spots on the surface of the nanoflakes with a size of 5–10 nm can be ascribed to be Ag NPs (Fierascu et al., 2018) (Fig. 2b). The Ag NPs on FBPA1 are smaller than those on FBPA10 which may provide a larger active surface area for Ag NPs to interact with bacteria. Some nanocomposites on FBPA1 even show a core-shell structure with an Ag layer coating on the surface of Fe_3O_4 NPs (inner picture in Fig. 2a). The selected area electron diffraction (SAED) patterns in Fig. 2a and d recorded at one FBPA1 or FBPA10 nanoflake exhibited regular and clear diffraction rings, revealing the polycrystalline nature (Zhang et al., 2016). The lattice fringes of Ag ($d = 0.128$ nm) for FBPA1 and Ag ($d = 0.117$ nm) for FBPA10 were shown clearly in Fig. 2c and f.

Since the oxidation of silver is thermodynamically favored at room temperature ($\Delta G^0_{298} = -11.25$ kJ/mol) (Levard et al., 2012), an oxide layer (Ag_2O) on the surface of Ag NPs may dissolve in pure water ($K_{sp} = 4 \times 10^{-11}$) (Johnston et al., 2002), which results in the release of Ag^+. However, most of released Ag^+ ions are retained on the Ag NP surface because of the presence of a layer of adsorbed BH_4^- ions at their surface (Kim et al., 2007; Sachdeva et al., 2006), which was demonstrated by the decreasing ZP of FBPA1 (3.7 mV) and FBPA10 (−8.5 mV) with increasing Ag loading in comparison with FBP (12.1 mV). In addition, the Ag NPs were found uniformly distributed on FBP's surface which can be explained by two reasons: (1) the adsorbed BH_4^- ions on the surface of the Ag NPs helped

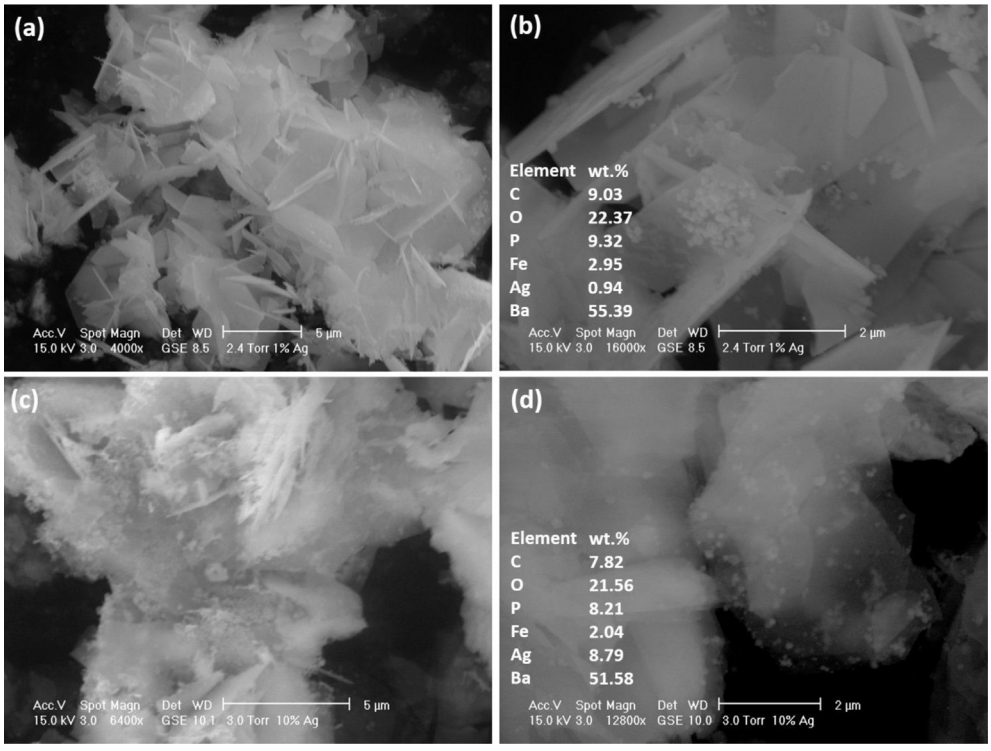

Fig. 1. SEM image, SEM close-up, and EDS results of (a, b) FBPA1 and (c, d) FBPA10.

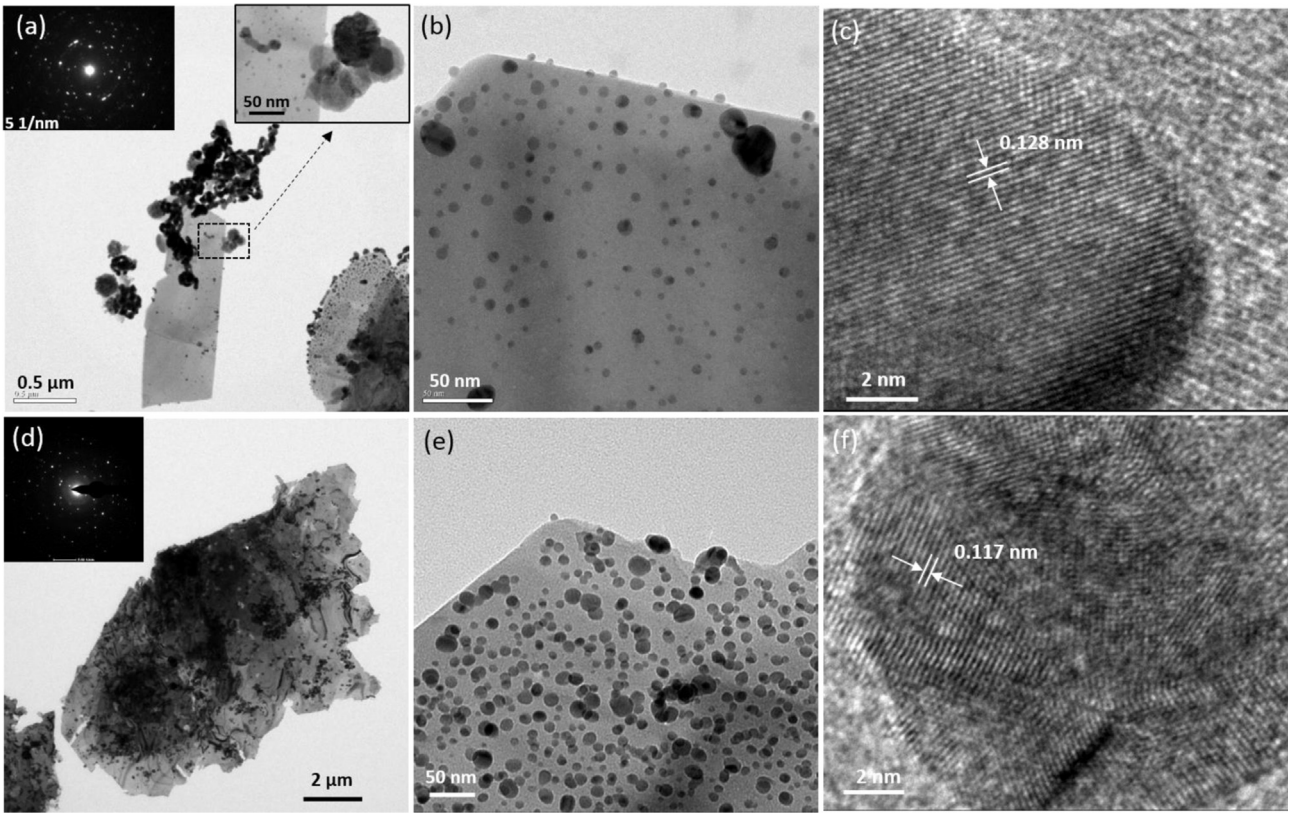

Fig. 2. (a, d) TEM image and SAED pattern, (b, e) TEM close-up, and (c, f) HRTEM of FBPA1 and FBPA10.

to separate and stabilize these NPs due to the repulsive forces between negatively charged Ag NPs (Mulfinger et al., 2007); and (2) loading of $Ag@Ag^{+}@BH_4^-$ on the positively charged FBP nanoflake (Ren et al., 2011; Song et al., 2018) can form an Ag-BH_4-FBP linkage, which can also help to stabilize the Ag NPs by avoiding the hydrolysis of BH_4^- ions (Pacioni et al., 2015). Therefore, no external stabilizing agent was needed to stabilize Ag NPs, which results in a more simple and cost-effective preparation process.

As seen from XRD data (Fig. 3a), the main characteristic peaks of FBP, FBPA1, and FBPA10 can be ascribed to the diffraction of $Ba_3(PO_4)_2$ (JCPDS No. 25-0028) (Zhang et al., 2012). The sharp peaks revealed the fine crystallinity of these materials (Zhang et al., 2012). The low concentration of Fe_3O_4 in these composites was confirmed by the small peaks at 35.8° (Zhang et al., 2014). There was no obvious difference in XRD patterns between FBP and FBPA1 except for two small peaks (marked arrow) in FBPA1 ascribed to Ag NPs (Ma et al., 2015; Reddy et al., 2007). As silver concentration increased to 10 wt%, a more characteristic pattern for metallic silver (38.4° and 64.6°) can be observed in XRD patterns of FBPA10 (Bethke and Kung, 1997), which suggested that silver atoms are not incorporating into the lattice of FBPA10 (or only to a very limited extent) but rather form on the surface of FBPA10 (Height et al., 2006).

As shown in Fig. 3b, there was no obvious change in the FT-IR spectra of FBP, FBPA1, and FBPA10. The strong and wide peak at 976 cm^{-1} contributed to the symmetric stretching vibration of PO_4^{3-} groups (Tank et al., 2013). The small peak at 1409 cm^{-1} can be ascribed to stretching vibration of $H_2PO_4^-$ groups. The relative decrease of these two peaks compared to pristine FBP suggested the homogeneous deposition of Ag NPs on the FBP surface (Zhu et al., 2012). Noticeably, no shifts in the characteristic bands of FBP were observed after Ag NP loading, indicating these Ag NPs are held via van der Waals and/or other weak interactions (Zhu et al., 2012). Similar interactions were also reported for silver-iron oxide NPs on the surface of fly ash (Zhu et al., 2012) and TiO_2-deposited FA materials (Wang et al., 2012).

As shown in Fig. 3c, the magnetic saturation (*Ms*) of FBPA1 (3.9 emu/g) and FBPA10 (3.1 emu/g) decreased with increased silver loading, in comparison with FBP (8.7 emu/g). However, the magnetic response was still strong enough to ensure easy and fast separation of FBPA1 and FBPA10 from solution by a common magnet.

XPS spectra of survey scans and high-resolution scans for the key elements on the surface of FBPA1, compared with FBP, are shown in Fig. 4 and Fig. S3. As shown in Fig. 4a, silver is newly detected in FBPA1 which was absent in FBP, demonstrating the existence of Ag on the surface of FBPA1. As shown in Fig. 4b, the difference between the Ag $3d_{3/2}$ (373.8 eV) and Ag $3d_{5/2}$ (367.8 eV) peaks (Ma et al., 2015) is 6.0 eV which is exactly the same as the value for metallic silver. This suggests that the majority of the silver atoms on FBPA1 exist in a zero valent state (Han et al., 1998; Shahid et al., 2018). After the calibration of C 1*s* which had eliminated the errors induced by the fitting and measurement, no obvious shifts in binding energy values for Ba 3*d*, O 1*s*, Fe 2*p*, and P 2*p* (Fig. S3) were observed between FBP and FBP1. This indicates that these elements are in a similar chemical environment (Zhu et al., 2007), and confirms that the loaded Ag NPs on FBPA1 are held mainly through van der Waals and/or other weak interactions (Zhu et al., 2012).

3.2. Adsorption and disinfection efficiency for E. coli

As shown in Fig. S4, the as-prepared FBP, FBPA1, and FBPA10 all showed obvious adsorption effects toward *E. coli* within 10 min with an order of FBP (97%) > FBPA1 (91%) > FBPA10 (83%). The

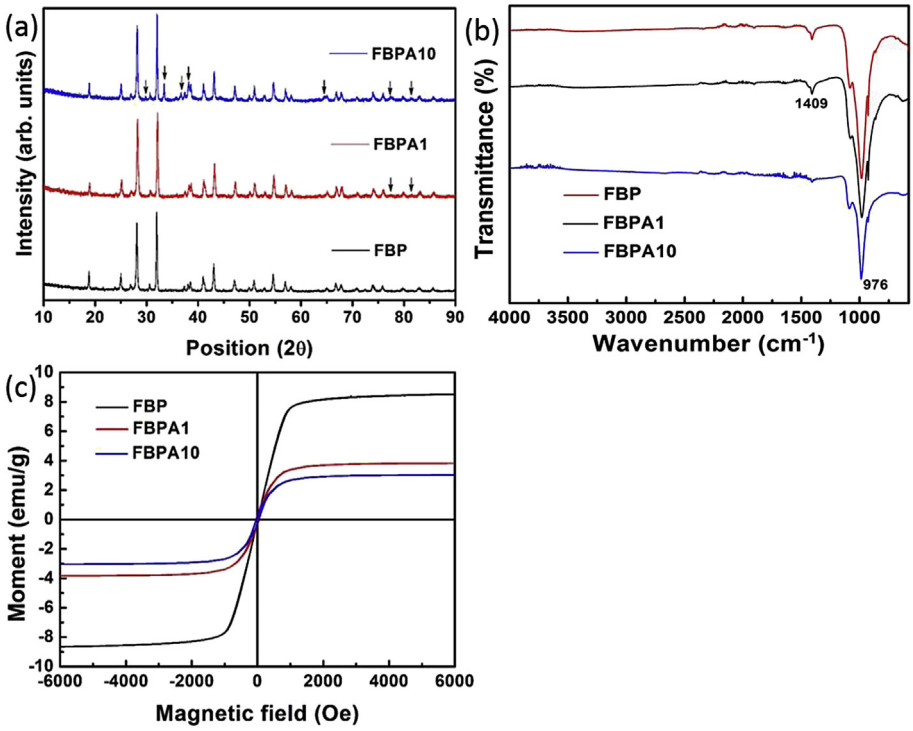

Fig. 3. (a) XRD patterns, (b) FT-IR spectra, and (c) magnetic properties of FBPA1 and FBPA10 in comparison with FBP.

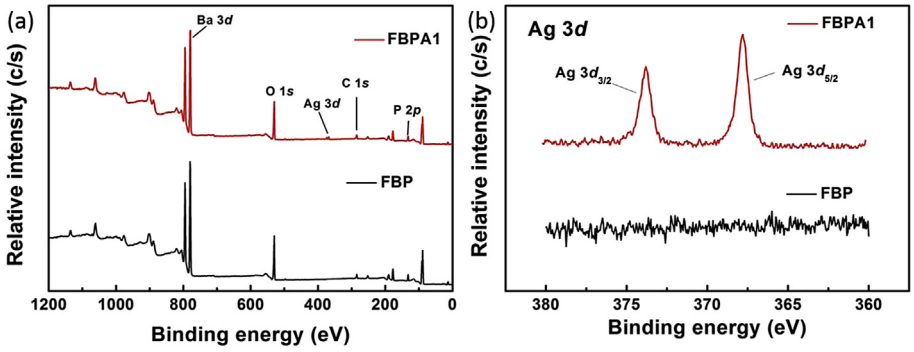

Fig. 4. XPS spectra of (a) survey scan and (b) Ag 3*d* for FBPA1 and FBP.

decreased adsorption efficiency with the increased Ag loading may be due to the increased repulsion force between loaded negatively charged Ag NPs (−0.86 mV) (Kim et al., 2007) and negatively charged *E. coli* (−17.1 mV). However, FBPA1 and FBPA10 showed a much higher disinfection efficiency (~100%) within 10 min than FBP (Fig. 5) and the calculated disinfection capacities were higher than other previous reported materials (Table S1). Therefore, the Ag NPs on the material were mainly responsible for the enhanced disinfection effect. And the loading of 1 wt% Ag NPs on FBP was sufficient to greatly enhance the disinfection efficiency of FBP for *E. coli* suspension with a concentration of 5×10^8 CFU/mL while the adsorption efficiency only showed a slight decrease. In addition, FBPA1 could be considered more promising for treating highly *E. coli* polluted water than FBPA10 due to the lower material cost.

Different parameters, such as pH, temperature, the dosage of material, and reaction time, which may affect the adsorption and disinfection efficiency by FBPA1 were investigated in detail and presented in Fig. 6. The higher disinfection efficiency at lower pH and higher temperature can be contributed to the increased release of silver (Han et al., 1998). However, pH and temperature had slighter effects on the adsorption efficiency compared with disinfection efficiency, as the adsorption for *E. coli* by FBPA1 was a complicated process which can be affected by various parameters, such as ZP, stability, and surface area of the nanocomposites. Therefore, no strict pH and temperature control were needed for *E. coli* adsorption which is beneficial to the practical application. As seen in Fig. 6c, a higher dosage of material can provide more effective adsorption sites and released silver for *E. coli* removal. Therefore, the adsorption and disinfection efficiency improved as material dosage increased. It was also observed that the adsorption and disinfection efficiency increased gradually with the extension of reaction time. And the disinfection process by FBPA1 was fast that almost all the bacteria cells were inactivated within 10 min.

After treatment, the high recovery rate of the *E. coli*-loaded materials (~99%) within 1 min (Fig. S4) by magnetic field would avoid potential secondary pollution to the water system. The FTIR

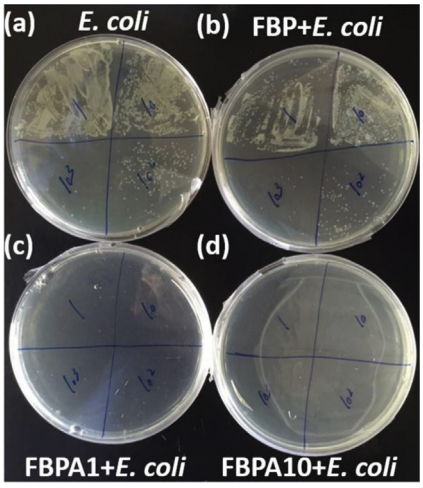

Fig. 5. Dilution plating procedure results with a dilution ratio of 1, 10, 10^2, and 10^3 after disinfection by FBPA1 and FBPA10 compared with FBP ($C_0 = 5 \times 10^8$ CFU/mL, 50 mL, material's dosage of 0.05 g, 25 °C, pH 6, 10 min).

spectra of FBPA1 after removing *E. coli* is presented in Fig. S5. A newly found peak at 1652 cm^{-1} in the recovered FBPA1 may be ascribed to the amide I group (C—O stretching along the N—H deformation) of proteins and peptides (Haldorai et al., 2015; Ojeda et al., 2008), and the increased peak at 1409 cm^{-1} can be assigned to C—O of deprotonated carboxylic groups (Jiang et al., 2016; Ojeda et al., 2008). These characteristic peaks of cells demonstrate the presence of *E. coli* on FBPA1 after adsorption. The obvious shift to the higher wavenumber of these two peaks in comparison with pristine bacteria (1647 and 1402 cm^{-1}) (Ojeda et al., 2008) can be contributed to the chemical interaction between cells and the nanomaterials.

3.3. Disinfection mechanism for E. coli

In order to investigate the enhanced disinfection effect by FBPA1 and FBPA10 in comparison with FBP, fluorescent-based cell tests of *E. coli* cells after 5 min were conducted (Fig. 7). Live and dead bacteria cells were represented by the heavy green fluorescence intensity region (Fig. 7a, d, and g), and the dead fraction of *E. coli* cells was indicated by the strong red fluorescence intensity region (Fig. 7b, e, and h) (Ma et al., 2015). The disinfection process was fast: within 5 min, ~23%, ~81%, and ~92% of *E. coli* can be inactivated by FBP, FBPA1, and FBPA10, respectively (Fig. 7c, f, and i). The greatly increased disinfection efficiency of FBPA1 and FBPA10 compared to FBP can be attributed to the well-known inhibitory and bactericidal properties of Ag NPs (Lee et al., 2005), which can (1) lead to permeability and respiration malfunctions of bacterial cell membrane (Markova et al., 2013); (2) induce the formation of free radicals which cause membrane damage (Ma et al., 2015); (3) penetrate inside the bacteria, and subsequently release Ag^+ with inactivation effect for proteins (Klueh et al., 2000; Kumar et al., 2005). The inactivated bacteria numbers treated by FBPA1 (4.1×10^8 CFU) and FBPA10 (4.6×10^8 CFU) are much higher than that by stabilized Ag NPs in Ma's (Ma et al., 2015) (10^7 CFU) and Sondi's (Sondi and Salopek-Sondi, 2004) (10^6 CFU) reports at the same dosage of 0.05 g. This can be ascribed to the FBP substrate, which can (1) capture more negatively charged bacteria to the planar surface of FBP through electrostatic interaction (Song et al., 2018); (2) cause irreversible cell structural damage by the sharp edges and corners of FBP (Song et al., 2018), promoting the inactivation effect of released Ag^+ for proteins inside the cells.

To further study the improved disinfection mechanism of FBPA1, the leaching of silver from FBPA1 was monitored via ICP-MS. After suspending 0.05 g FBPA1 in 50 mL of DI water for 24 h, 0.06 ± 0.01 mg/L of Ag^+ was found released into solution, which was lower than the current regulatory limit (0.1 mg/L) of the U.S. Environmental Protection Agency (EPA) for drinking water. After

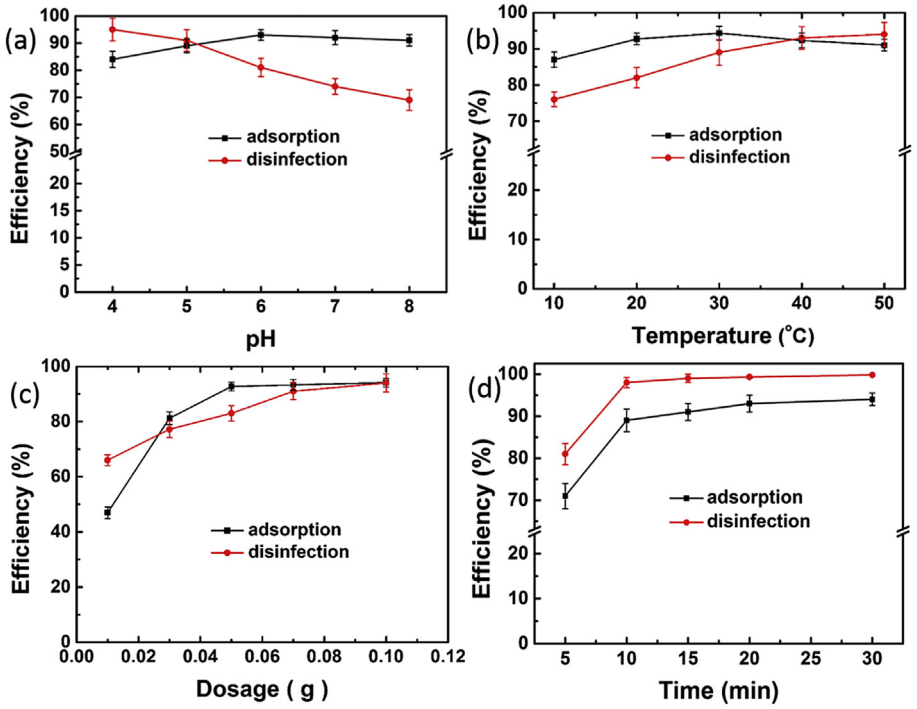

Fig. 6. The adsorption and disinfection efficiency of *E. coli* from solution by FBPA1 at different (a) pH, (b) temperature, (c) dosage, and (d) reaction time ($C_0 = 5 \times 10^8$ CFU/mL, 50 mL, material's dosage of 0.05 g, 25 °C, pH 6, reaction time of 10 min).

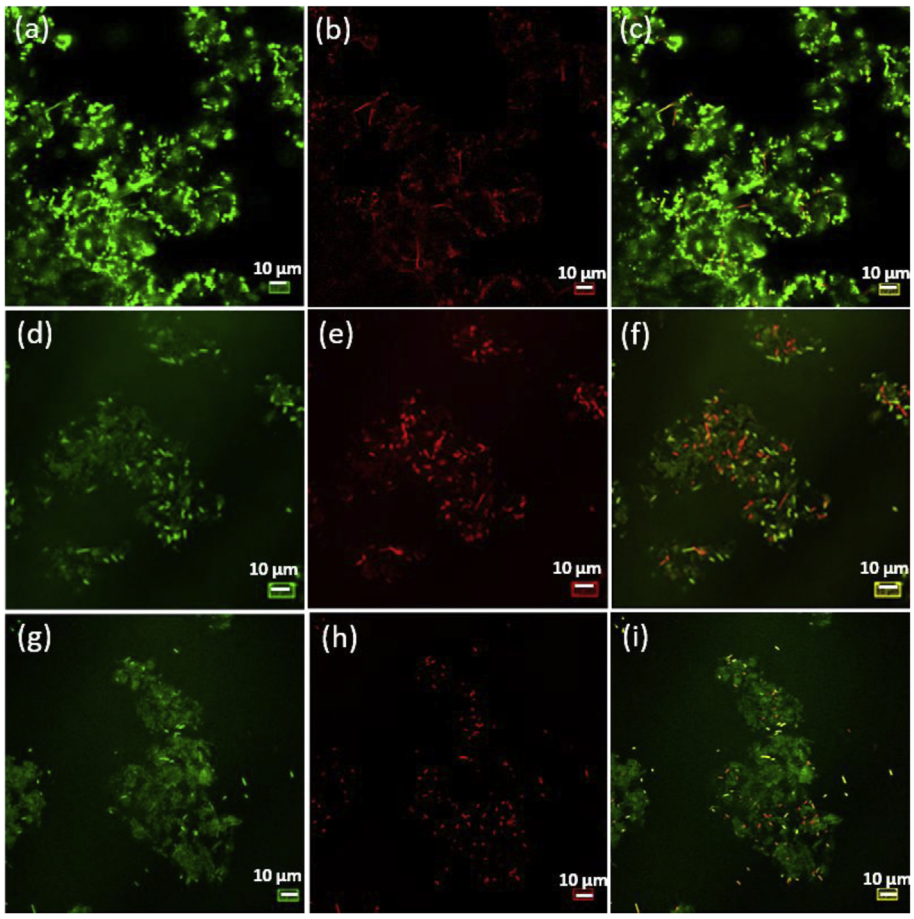

Fig. 7. Confocal fluorescent images of *E. coli* cells ($C_0 = 5 \times 10^8$ CFU/mL) stained with SYTO9 (green, live and dead) and PI (red, dead) after being treated with 0.05 g of (a–c) FBP, (d–f) FBPA1, and (g–i) FBPA10 in pH 6.0 solutions for 5 min at 25 °C, and (c, f, i) Overlying images of bacterial cells stained with SYTO9 and PI.

the cell membrane is damaged by the sharp edges of FBP nanoflakes (Song et al., 2018) and Ag NPs (Kim et al., 2007; Kumar et al., 2005; Markova et al., 2013), these released silver ions can inactivate proteins and/or intercalate between the purine and pyrimidine bases of DNA (Klueh et al., 2000), leading to improved disinfection in comparison with FBP.

3.4. Effects of co-existing ions on the disinfection process

The disinfection efficiency of FBPA1 in the presence of common ions (from $CaCl_2$, $MgCl_2$, and NaCl) in water was investigated by confocal fluorescent images (Fig. 8). The calculated disinfection efficiency of FBPA1 at the co-existence of $CaCl_2$, $MgCl_2$, and NaCl followed the order of NaCl (~67%)> $CaCl_2$ (~59%) > $MgCl_2$ (~41%), which were all lower than that without co-existing ions (~81%, Fig. 7d–f). Therefore, higher material dosage will be needed to treat the water with high salinity. Pure Ca^{2+}, Mg^{2+}, and Na^+ ions showed much lower disinfection effectiveness than Ag^+ (Fig. S9). Therefore, they made a weak contribution to the disinfection efficiency. On the other hand, the concentrations of these cation ions were decreased from 2 mg/L to 1.1–1.3 mg/L after treatment, indicating that they may be adsorbed on the surface of the negatively charged Ag NPs on FBP to form stable Ag–BH_4–Ca/Mg/Na linkages, as observed in another study (Sachdeva et al., 2006). These linkages may act as stabilizers onto the small Ag NPs (Sharma et al., 2017) and inhibit the leaching of Ag^+ (Table S2), leading to the decreased disinfection effect. Noticeable, $MgCl_2$ showed the strongest inhibition of Ag^+ leaching, followed by NaCl and $CaCl_2$ (Table S2). This may be due to the higher concentration of dissociated Cl^- ions from $MgCl_2$ than from NaCl and $CaCl_2$ at the same cation concentration of 2 mg/L, resulting in more insoluble AgCl precipitates covered the surface of Ag NPs and then the decreased release of silver (Levard et al., 2012).

3.5. Reusability of FBPA1

To provide a more economical disinfection approach, the reusability was tested. ~99% of the bacteria-loaded FBPA1 after disinfection can be recovered from the suspension using a magnet. As shown in Fig. S8a, some dead *E. coli* cells were newly found on the top of recycled FBPA1, and the sticky surface of material compared to pristine FBPA1 can be ascribed to the inner contents of the dead bacteria cells (Song et al., 2018). The reclaimed FBPA1 could be regenerated by DI water (Fig. S8b) and then reused for 5 cycles. The adsorption efficiency of *E. coli* by FBPA1 was 94% in the first cycle, and then decreased slowly after each cycle to 86% after 5 cycles (Fig. 9). The ZP of FBPA1 changed from 3.7 mV to −13.9 mV after the first treatment cycle, and then slightly decreased and eventually attained a ZP similar to *E. coli* (Fig. 9b). Therefore, the reuse of FBPA1 for five cycles resulted in a surface covered more and more by negatively charged *E. coli*, increasing the repulsive force and providing less available sites for other *E. coli* (Song et al., 2018). However, FBPA1 still removes around 86% of *E. coli* after five cycles, implying that the electrostatic interaction may be not the dominant mechanism for the high adsorption efficiency during the reuse (Song et al., 2018). Flocculation, hydrogen bonding, and magnetic aggregation may be also involved (Song et al., 2018).

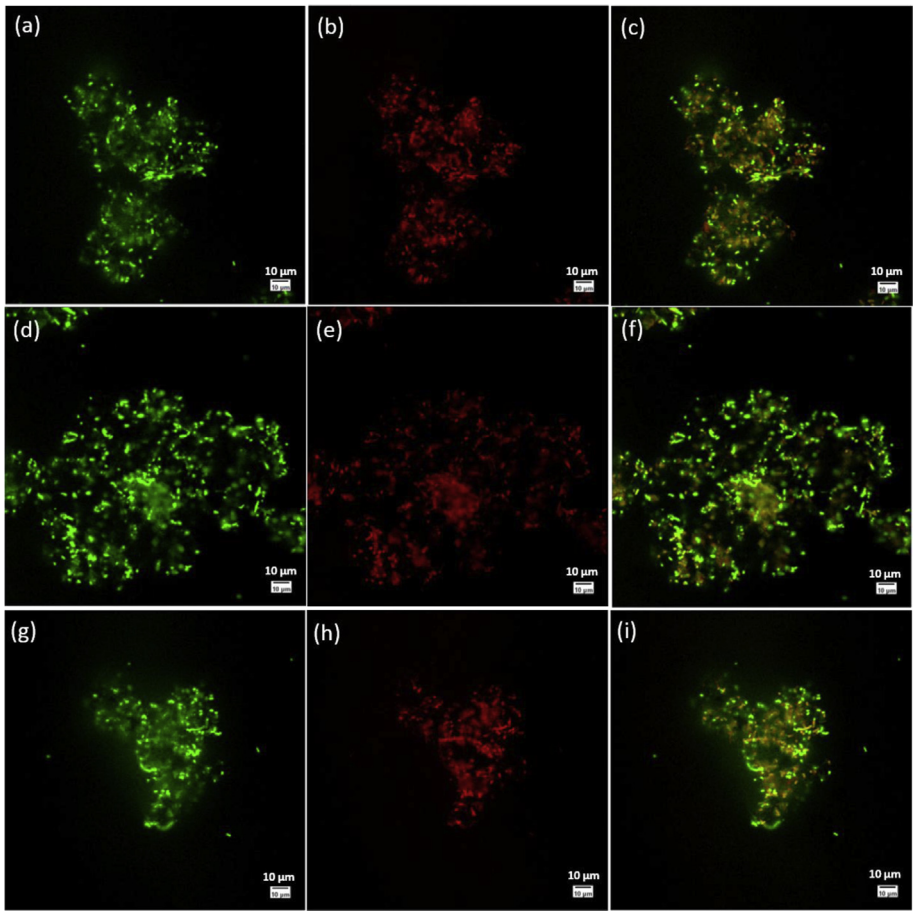

Fig. 8. Confocal fluorescent images of *E. coli* cells ($C_0 = 5 \times 10^8$ CFU/mL) after being treated by 0.05 g FBPA1 for 5 min at 25 °C in pH 6.0 solutions containing a cation concentration of 2 mg/L of (a–c) $CaCl_2$, (d–f) $MgCl_2$, or (g–i) NaCl. The cells were stained with SYTO9 (live and dead, green) and PI (dead, red). (c, f, i) Overlying images of *E. coli* stained with SYTO9 and PI.

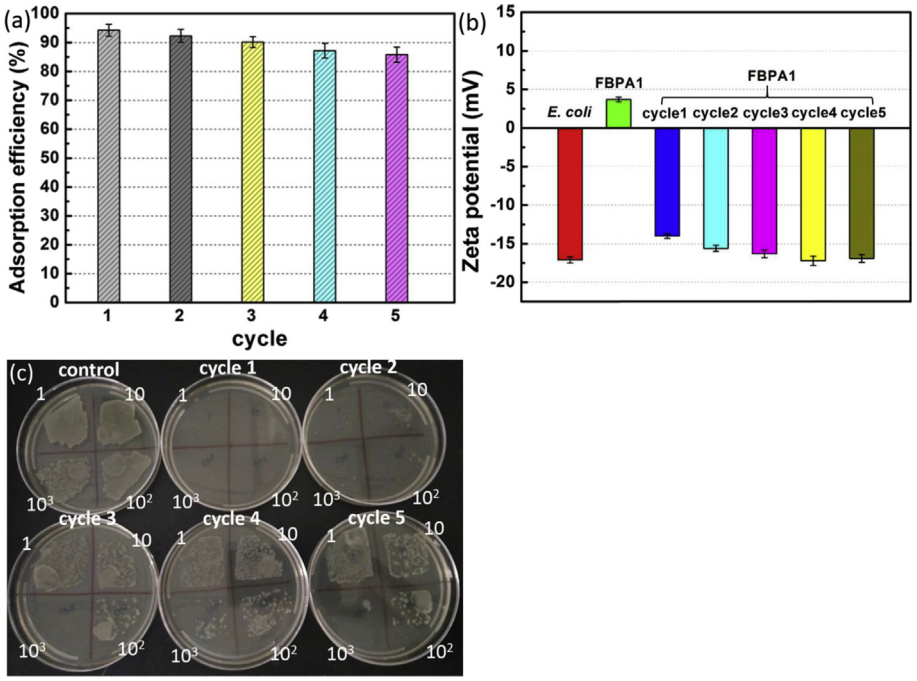

Fig. 9. (a) Adsorption efficiency for *E. coli* by FBPA1 at different cycle ($C_0 = 5 \times 10^8$ CFU/mL, 50 mL, material's dosage of 0.05 g, 25 °C, pH 6, reaction time of 10 min); (b) ZP of FBPA1 at different reuse cycles in comparison with *E. coli* and pristine FBPA1; (c) dilution plating procedure results with a dilution ratio of 1, 10, 10^2, and 10^3 after disinfection by FBPA1 at different cycle ($C_0 = 5 \times 10^6$ CFU/mL, 50 mL, material's dosage of 5 mg, 25 °C, pH 6, 30 min).

To treat the simulated wastewater using FBPA1, a low material dosage (0.1 g/L) was used to treat *E. coli* suspension with a concentration of 5×10^6 CFU/mL (pH 7) under stirring at 100 rpm for 30 min. Dilution plating results (Fig. 9c) showed high disinfection efficiency of FBPA1 in the first two using cycles, with a significant decrease in the following cycles. It could be due to the mass loss of FBPA1 in solution during the recovery and sampling process (2 mL mixed solution of FBPA1 and *E. coli* for plating experiment and ZP test at each cycle). Moreover, the decreased amount of leached Ag from FBPA1 increasingly covered with bacteria after additional cycles (Fig. S9) can also explain the decrease in disinfection efficacy of FBPA1 with time. However, on the basis of dilution plate count results (Fig. 9c), more than 70% of *E. coli* was inactivated by FBPA1 even in the third, fourth, and fifth reuse cycles, implying good reusability for disinfection application.

4. Conclusions

In this work, a simple method was developed to obtain Ag NPs loaded magnetic iron-oxide barium phosphate nanoflakes with a controllable content of ~1 wt% and ~10 wt% Ag NPs. The adsorption efficiency of *E. coli* by FBPA1 was higher than that of FBPA10, which may be due to a lower repulsion force between the negatively charged Ag NPs on FBPA1 and *E. coli*. The loading of Ag NPs on the material can improve the disinfection efficiency toward *E. coli*, leading to higher disinfection capacities of FBPA1 and FBPA10 than some other materials. The strong inactivation of the cell membrane and proteins by Ag NPs and leached Ag^+ was mainly responsible for the enhanced disinfection effect. However, the co-existence of $CaCl_2$, or $MgCl_2$, or NaCl in solution can inhibit the leaching of Ag^+ from FBPA1 by forming AgCl precipitation on Ag NPs, leading to a decreased disinfection efficiency. Higher material dosage will be needed to treat for the high salinity water. The magnetic properties of FBPA1 are a key advantage, since it allows a facile magnetic separation from suspension after treatment, avoiding the release of Ag NPs to the water supply. The recovered FBPA1 can be reused for at least five treatment cycles, maintaining good *E. coli* adsorption and disinfection. Due to the easy preparation, high adsorption efficiency, great disinfection control, and good recyclability, the novel Ag NPs loaded FBP composites in this work hold potential as preferred nanomaterials for water disinfection.

Acknowledgement

This work was supported by the National Natural Science Funds of China (No. 51402153), the Jiangsu Natural Science Funds of China (No. SBK2017020336), and the Fundamental Research Funds for the Central Universities (No. KYZ201747). This work was partly supported by the National Science Foundation and the U.S. Environmental Protection Agency under NSF-EF0830117. AAK also appreciates Agilent Technologies for their Agilent Thought Leader Award.

Appendix A. Supplementary data

Supplementary data to this article can be found online at https://doi.org/10.1016/j.jclepro.2019.01.232.

References

Bethke, K.A., Kung, H.H., 1997. Supported Ag catalysts for the lean reduction of NO with C3H6. J. Catal. 172, 93–102. https://doi.org/10.1006/jcat.1997.1794.

Boholm, M., Arvidsson, R., 2014. Controversy over antibacterial silver: implications for environmental and sustainability assessments. J. Clean. Prod. 68, 135–143. https://doi.org/10.1016/j.jclepro.2013.12.058.

Choi, O., Hu, Z., 2008. Size dependent and reactive oxygen species related nanosilver toxicity to nitrifying bacteria. Environ. Sci. Technol. 42, 4583–4588. https://doi.org/10.1021/es703238h.

Das, S.K., Khan, M.M.R., Parandhaman, T., Laffir, F., Guha, A.K., Sekarana, G., Mandal, A.B., 2013. Nano-silica fabricated with silver nanoparticles: antifouling adsorbent for efficient dye removal, effective water disinfection and biofouling control. Nanoscale 5, 5549–5560. https://doi.org/10.1039/c3nr00856h.

Elahifard, M.R., Rahimnejad, S., Haghighi, S., Gholami, M.R., 2007. Apatite-coated Ag/AgBr/TiO2 visible-light photocatalyst for destruction of bacteria. J. Am. Chem. Soc. 129, 9552–9553. https://doi.org/10.1021/ja072492m.

Fierascu, I., Fierascu, R.C., Somoghi, R., Ion, R.M., Moanta, A., Avramescu, S.M., Damian, C.M., Ditu, L.M., 2018. Tuned apatitic materials: Synthesis, characterization and potential antimicrobial applications. Appl. Surf. Sci. 438, 127–135. https://doi.org/10.1016/j.apsusc.2017.08.087.

Gupta, V.K., Agarwal, S., Tyagi, I., Pathania, D., Rathore, B.S., Sharma, G., 2015. Synthesis, characterization and analytical application of cellulose acetate-tin (IV) molybdate nanocomposite ion exchanger: binary separation of heavy metal ions and antimicrobial activity. Ionics (Kiel) 21, 2069–2078. https://doi.org/10.1007/s11581-015-1368-4.

Haldorai, Y., Kharismadewi, D., Tuma, D., Shim, J.-J., 2015. Properties of chitosan/magnetite nanoparticles composites for efficient dye adsorption and antibacterial agent. Kor. J. Chem. Eng. 32, 1688–1693. https://doi.org/10.1007/s11814-014-0368-9.

Han, S.W., Kim, Y., Kim, K., 1998. Dodecanethiol-derivatized Au/Ag bimetallic nanoparticles: TEM, UV/VIS, XPS, and FTIR analysis. J. Colloid Interface Sci. 208, 272–278. https://doi.org/10.1006/jcis.1998.5812.

Height, M.J., Pratsinis, S.E., Mekasuwandumrong, O., Praserthdam, P., 2006. Ag-ZnO catalysts for UV-photodegradation of methylene blue. Appl. Catal. B Environ. 63, 305–312. https://doi.org/10.1016/j.apcatb.2005.10.018.

Hwang, E.T., Lee, J.H., Chae, Y.J., Kim, Y.S., Kim, B.C., Sang, B.-I., Gu, M.B., 2008. Analysis of the toxic mode of action of silver nanoparticles using stress-specific bioluminescent bacteria. Small 4, 746–750. https://doi.org/10.1002/smll.200700954.

Inbaraj, B.S., Tsai, T.-Y., Chen, B.-H., 2012. Synthesis, characterization and antibacterial activity of superparamagnetic nanoparticles modified with glycol chitosan. Sci. Technol. Adv. Mater. 13. https://doi.org/10.1088/1468-6996/13/1/015002.

Jiang, Y., Gong, J.L., Zeng, G.M., Ou, X.M., Chang, Y.N., Deng, C.H., Zhang, J., Liu, H.Y., Huang, S.Y., 2016. Magnetic chitosan-graphene oxide composite for antimicrobial and dye removal applications. Int. J. Biol. Macromol. 82, 702–710.

Johnston, H.L., Cuta, F., Garrett, A.B., 2002. The solubility of silver oxide in water, in alkali and in alkaline salt solutions. The amphoteric character of silver hydroxide. J. Am. Chem. Soc. 55, 2311–2325.

Joshi, M.K., Pant, H.R., Liao, N., Kim, J.H., Kim, H.J., Park, C.H., Kim, C.S., 2015. In-situ deposition of silver-iron oxide nanoparticles on the surface of fly ash for water purification. J. Colloid Interface Sci. 453, 159–168. https://doi.org/10.1016/j.jcis.2015.04.044.

Kim, J.S., Kuk, E., Yu, K.N., Kim, J.-H., Park, S.J., Lee, H.J., Kim, S.H., Park, Y.K., Park, Y.H., Hwang, C.-Y., Kim, Y.-K., Lee, Y.-S., Jeong, D.H., Cho, M.-H., 2007. Antimicrobial effects of silver nanoparticles. Nanomed. Nanotechnol. Biol. Med. 3, 95–101. https://doi.org/10.1016/j.nano.2006.12.001.

Klueh, U., Wagner, V., Kelly, S., Johnson, A., Bryers, J.D., 2000. Efficacy of silver-coated fabric to prevent bacterial colonization and subsequent device-based biofilm formation. J. Biomed. Mater. Res. 53, 621–631 https://doi.org/10.1002/1097-4636(2000)53:6<621::aid-jbm2>3.0.co;2-q.

Kolmas, J., Groszyk, E., Kwiatkowska-Rozycka, D., 2014. Substituted Hydroxyapatites with Antibacterial Properties. BioMed Res. Int. https://doi.org/10.1155/2014/178123.

Kumar, R., Howdle, S., Munstedt, H., 2005. Polyamide/silver antimicrobials: Effect of filler types on the silver ion release. J. Biomed. Mater. Res. B Appl. Biomater. 75B, 311–319. https://doi.org/10.1002/jbm.b.30306.

Kumar, R., Munstedt, H., 2005. Silver ion release from antimicrobial polyamide/silver composites. Biomaterials 26, 2081–2088. https://doi.org/10.1016/j.biomaterials.2004.05.030.

Lee, D., Cohen, R.E., Rubner, M.F., 2005. Antibacterial properties of Ag nanoparticle loaded multilayers and formation of magnetically directed antibacterial microparticles. Langmuir 21, 9651–9659. https://doi.org/10.1021/la0513306.

Levard, C., Hotze, E.M., Lowry, G.V., Brown Jr., G.E., 2012. Environmental transformations of silver nanoparticles: impact on stability and toxicity. Environ. Sci. Technol. 46, 6900–6914. https://doi.org/10.1021/es2037405.

Ma, N., Zhang, Y., Quan, X., Fan, X., Zhao, H., 2010. Performing a microfiltration integrated with photocatalysis using an Ag-TiO2/HAP/Al2O3 composite membrane for water treatment: Evaluating effectiveness for humic acid removal and anti-fouling properties. Water Res. 44, 6104–6114. https://doi.org/10.1016/j.watres.2010.06.068.

Ma, S., Zhan, S., Jia, Y., Zhou, Q., 2015. Highly efficient antibacterial and Pb(II) removal effects of Ag-CoFe2O4-GO nanocomposite. ACS Appl. Mater. Interfaces 7, 10576–10586. https://doi.org/10.1021/acsami.5b02209.

Markova, Z., Siskova, K.M., Filip, J., Cuda, J., Kolar, M., Safarova, K., Medrik, I., Zboril, R., 2013. Air stable magnetic bimetallic Fe-Ag nanoparticles for advanced antimicrobial treatment and phosphorus removal. Environ. Sci. Technol. 47, 5285–5293. https://doi.org/10.1021/es304693g.

Mulfinger, L., Solomon, S.D., Bahadory, M., Jeyarajasingam, A.V., Rutkowsky, S.A., Boritz, C., 2007. Synthesis and study of silver nanoparticles. J. Chem. Educ. 84, 322.

Ojeda, J.J., Romero-Gonzalez, M.E., Bachmann, R.T., Edyvean, R.G.J., Banwart, S.A., 2008. Characterization of the cell surface and cell wall chemistry of drinking

water bacteria by combining XPS, FTIR spectroscopy, modeling, and potentiometric titrations. Langmuir 24, 4032–4040. https://doi.org/10.1021/la702284b.
Pacioni, N.L., Borsarelli, C.D., Rey, V., Veglia, A.V., 2015. Synthetic routes for the preparation of silver nanoparticles. Silver Nanoparticle Appl. 13–46.
Ratte, H.T., 1999. Bioaccumulation and toxicity of silver compounds: A review. Environ. Toxicol. Chem. 18, 89–108 https://doi.org/10.1897/1551-5028(1999)018<0089:batosc>2.3.co;2.
Ravi, N.D., Balu, R., Kumar, T.S.S., 2012. Strontium-substituted calcium deficient hydroxyapatite nanoparticles: synthesis, characterization, and antibacterial properties. J. Am. Ceram. Soc. 95, 2700–2708. https://doi.org/10.1111/j.1551-2916.2012.05262.x.
Raza, Z.A., Rehman, A., Mohsin, M., Bajwa, S.Z., Anwar, F., Naeem, A., Ahmad, N., 2015. Development of antibacterial cellulosic fabric via clean impregnation of silver nanoparticles. J. Clean. Prod. 101, 377–386. https://doi.org/10.1016/j.jclepro.2015.03.091.
Reddy, M.P., Venugopal, A., Subrahmanyam, M., 2007. Hydroxyapatite-supported Ag-TiO2 as *Escherichia coli* disinfection photocatalyst. Water Res. 41, 379–386. https://doi.org/10.1016/j.watres.2006.09.018.
Ren, W., Fang, Y., Wang, E., 2011. A binary functional substrate for enrichment and ultrasensitive sers spectroscopic detection of folic acid using graphene oxide/Ag nanoparticle hybrids. ACS Nano 5, 6425–6433. https://doi.org/10.1021/nn201606r.
Sachdeva, A., Sodaye, S., Pandey, A.K., Goswami, A., 2006. Formation of silver nanoparticles in poly(perfluorosulfonic) acid membrane. Anal. Chem. 78, 7169–7174. https://doi.org/10.1021/ac060647n.
Schwarzenbach, R.P., Escher, B.I., Fenner, K., Hofstetter, T.B., Johnson, C.A., von Gunten, U., Wehrli, B., 2006. The challenge of micropollutants in aquatic systems. Science 313, 1072–1077. https://doi.org/10.1126/science.1127291.
Sedlak, D.L., von Gunten, U., 2011. The chlorine dilemma. Science 331, 42–43. https://doi.org/10.1126/science.1196397.
Shahid, M., Zhou, Y., Cheng, X.-W., Zar, M.S., Chen, G., Tang, R.-C., 2018. Ferulic acid promoted in-situ generation of AgNPs@silk as functional colorants. J. Clean. Prod. 176, 736–744. https://doi.org/https://doi.org/10.1016/j.jclepro.2017.12.171.
Sharma, G., Kumar, A., Naushad, M., Kumar, A., Al-Muhtaseb, A.H., Dhiman, P., Ghfar, A.A., Stadler, F.J., Khan, M.R., 2018. Photoremediation of toxic dye from aqueous environment using monometallic and bimetallic quantum dots based nanocomposites. J. Clean. Prod. 172, 2919–2930. https://doi.org/https://doi.org/10.1016/j.jclepro.2017.11.122.
Sharma, G., Kumar, D., Kumar, A., Al-Muhtaseb, A.H., Pathania, D., Naushad, M., Mola, G.T., 2017. Revolution from monometallic to trimetallic nanoparticle composites, various synthesis methods and their applications: A review. Mater. Sci. Eng. C 71, 1216–1230. https://doi.org/https://doi.org/10.1016/j.msec.2016.11.002.
Sharma, V.K., McDonald, T.J., Kim, H., Garg, V.K., 2015. Magnetic graphene-carbon nanotube iron nanocomposites as adsorbents and antibacterial agents for water purification. Adv. Colloid Interface Sci. 225, 229–240. https://doi.org/10.1016/j.cis.2015.10.006.
Singh, S., Bahadur, D., 2015. Catalytic and antibacterial activity of Ag decorated magnetic core shell nanosphere. Colloids Surfaces B Biointerfaces 133, 58–65. https://doi.org/10.1016/j.colsurfb.2015.05.033.
Singh, S., Barick, K.C., Bahadur, D., 2011. Surface engineered magnetic nanoparticles for removal of toxic metal ions and bacterial pathogens. J. Hazard. Mater. 192, 1539–1547. https://doi.org/10.1016/j.jhazmat.2011.06.074.
Sondi, I., Salopek-Sondi, B., 2004. Silver nanoparticles as antimicrobial agent: a case study on E-coli as a model for Gram-negative bacteria. J. Colloid Interface Sci. 275, 177–182. https://doi.org/10.1016/j.jcis.2004.02.012.
Song, B., Zhang, C., Zeng, G., Gong, J., Chang, Y., Jiang, Y., 2016. Antibacterial properties and mechanism of graphene oxide-silver nanocomposites as bactericidal agents for water disinfection. Arch. Biochem. Biophys. 604, 167–176. https://doi.org/https://doi.org/10.1016/j.abb.2016.04.018.
Song, J., Zhang, F., Huang, Y., Keller, A.A., Tang, X., Zhang, W., Jia, W., Santos, J., 2018. Highly efficient bacterial removal and disinfection by magnetic barium phosphate nanoflakes with embedded iron oxide nanoparticles. Environ. Sci. 5, 1341–1349. https://doi.org/10.1039/c8en00403j.
Tank, K.P., Chudasama, K.S., Thaker, V.S., Joshi, M.J., 2013. Cobalt-doped nanohydroxyapatite: synthesis, characterization, antimicrobial and hemolytic studies. J. Nanoparticle. Res. 15. https://doi.org/10.1007/s11051-013-1644-z.
Thakur, M., Sharma, G., Ahamad, T., Ghfar, A.A., Pathania, D., Naushad, M., 2017. Efficient photocatalytic degradation of toxic dyes from aqueous environment using gelatin-Zr(IV) phosphate nanocomposite and its antimicrobial activity. Colloids Surfaces B Biointerfaces 157, 456–463.
Tran, N., Mir, A., Mallik, D., Sinha, A., Nayar, S., Webster, T.J., 2010. Bactericidal effect of iron oxide nanoparticles on Staphylococcus aureus. Int. J. Nanomed. 5, 277–283.
Wang, B., Li, C., Pang, J., Qing, X., Zhai, J., Li, Q., 2012. Novel polypyrrole-sensitized hollow TiO2/fly ash cenospheres: Synthesis, characterization, and photocatalytic ability under visible light. Appl. Surf. Sci. 258, 9989–9996. https://doi.org/10.1016/j.apsusc.2012.06.061.
Yin, L., Cheng, Y., Espinasse, B., Colman, B.P., Auffan, M., Wiesner, M., Rose, J., Liu, J., Bernhardt, E.S., 2011. More than the ions: the effects of silver nanoparticles on *Lolium multiflorum*. Environ. Sci. Technol. 45, 2360–2367. https://doi.org/10.1021/es103995x.
Zhan, S., Zhu, D., Ma, S., Yu, W., Jia, Y., Li, Y., Yu, H., Shen, Z., 2015. Highly efficient removal of pathogenic bacteria with magnetic graphene composite. ACS Appl. Mater. Interfaces 7, 4290–4298. https://doi.org/10.1021/am508682s.
Zhang, F., Shi, Y., Zhao, Z., Song, W., Cheng, Y., 2014. Influence of semiconductor/insulator/semiconductor structure on the photo-catalytic activity of Fe3O4/SiO2/polythiophene core/shell submicron composite. Appl. Catal. B Environ. 150, 472–478. https://doi.org/10.1016/j.apcatb.2013.12.049.
Zhang, F., Yin, X., Zhang, W., 2016. Development of magnetic Sr-5(PO4)(3)(OH)/Fe3O4 nanorod for adsorption of Congo red from solution. J. Alloy. Comp. 657, 809–817. https://doi.org/10.1016/j.jallcom.2015.10.178.
Zhang, F., Zhao, Z., Tan, R., Guo, Y., Cao, L., Chen, L., Li, J., Xu, W., Yang, Y., Song, W., 2012. Selective and effective adsorption of methyl blue by barium phosphate nano-flake. J. Colloid Interface Sci. 386, 277–284. https://doi.org/10.1016/j.jcis.2012.07.034.
Zhu, L., He, C., Huang, Y., Chen, Z., Xia, D., Su, M., Xionga, Y., Li, S., Shu, D., 2012. Enhanced photocatalytic disinfection of *E. coli* 8099 using Ag/BiOI composite under visible light irradiation. Separ. Purif. Technol. 91, 59–66. https://doi.org/10.1016/j.seppur.2011.10.026.
Zhu, X., Fan, H., Li, D., Xiao, Y., Zhang, X., 2007. Protein adsorption and zeta potentials of a biphasic calcium phosphate ceramic under various conditions. J. Biomed. Mater. Res. B Appl. Biomater. 82B, 65–73. https://doi.org/10.1002/jbm.b.30706.